Journal of The Electrochemical Society, **157** (3) P18-P22 (2010)
0013-4651/2010/157(3)/P18/5/$28.00 © The Electrochemical Society

Ni Inverse Opals for Water Electrolysis in an Alkaline Electrolyte

Yi-Jui Huang, Chun-Han Lai, Pu-Wei Wu,[*,z] and Li-Yin Chen

Department of Materials Science and Engineering, National Chiao Tung University, Hsinchu 300, Taiwan

A vertical electrophoretic deposition technique was employed to prepare polystyrene (PS) colloidal crystals with negligible crystallographic defects. The colloidal crystals were plated with Ni, followed by selective removal of PS microspheres to fabricate inverse opals. With adjustments in relevant processing parameters, we were able to obtain inverse opals in multiple layers with excellent surface uniformities. The inverse opals were used as the electrode material for water electrolysis. Results from current–potential polarizations in 1 M KOH aqueous solution indicated that the catalytic abilities for oxygen evolution reaction (OER) and hydrogen evolution reaction (HER) increased with the layers of inverse opals. Estimation of the effective current densities determined that the entire area of the inverse opals was available for electrochemical reactions. In galvanostatic measurements for both OER and HER, the inverse opals demonstrated stable voltage profiles without notable degradations for 120 h. Compared with a planar Ni plate, the inverse opals exhibited a significantly reduced overpotential for the water electrolysis.
 [DOI: 10.1149/1.3281332]

Manuscript submitted July 29, 2009; revised manuscript received November 30, 2009. Published January 19, 2010.

The production of hydrogen is of particular interest because hydrogen is considered as a clean fuel for CO_2-free electricity. To date, production methods including chemical reactions, bioconversions, and water electrolysis have been studied with impressive results.[1-3] Among them, water electrolysis has attracted significant attention because of its simple setup and scaling. Water electrolysis entails an externally applied voltage to split the water into hydrogen and oxygen.[4,5] This process is energy-consuming because both the oxygen evolution reaction (OER) and hydrogen evolution reaction (HER) involve a substantial polarization loss. Hence, electrocatalysts are employed to reduce overpotentials at both electrodes. For example, oxides such as $Cu_xCo_{3-x}O_4$ and MnO_x are evaluated for the OER, and metals including Mo and Pt are used for the HER.[6-9] However, because of low cost and reasonable chemical stability, Ni and its alloys have become promising candidates as electrodes and catalyst supports for industrial water electrolysis.[10,11]

In addition to the development of unique electrocatalysts, an alternative approach to enhance both OER and HER is to prepare the electrodes with excessive surface areas. This can be achieved via the construction of metallic inverse opals with proper porosities and layer/thickness. To fabricate metallic inverse opals, an assembly of microspheres made of silica or polystyrene (PS) is often conducted first to produce colloidal crystals, followed by electrochemical or chemical depositions to fill desirable metals within the interstitial voids among those close-packed microspheres.[12,13] The encapsulated microspheres can be selectively removed, leaving metal skeletons as the inverse opals. So far, many papers have delineated the preparations of metallic inverse opals for photonic, sensing, and electrochemical devices.[14-16] However, the exploration of metallic inverse opals for water electrolysis has not been reported yet.

The other possibility to increase the surface area of an electrode is to prepare a porous structure made of metal powders. Despite the recent fabrications of colloidal crystals by electrophoretic deposition of metal powders,[17-19] their prospects in the application for water electrolysis are not promising. In comparison with widely used colloidal microspheres such as SiO_2 and PS, the metal exhibits a large mass density, which makes it difficult to disperse, suspend, and migrate in electrophoresis. Hence, the existing examples of electrophoretic deposition involve the metal powders with size less than 80 nm, and their deposition rates are usually slow. In addition, the interstitial voids among the metal powders are rather small and might not be interconnected. These attributes are not conductive to water electrolysis because the mass transport of water and bubbles (O_2/H_2) requires sufficient spaces to proceed. Moreover, the packed metal powders lack adequate mechanical strength because the interparticle bonding among them is physical in nature. Hence, upon the release of gas bubbles, it is expected that the packed metal powders would disintegrate into pieces and cease to function.

Recently, we have demonstrated the construction of large-area colloidal crystals and their inverse opals with excellent surface uniformity and reduced crystallographic defects by electrophoresis in a vertical arrangement.[20,21] In this work, we fabricate the Ni inverse opals at controlled layers and evaluate their electrochemical characteristics for the OER and HER in an alkaline electrolyte.

Experimental

The synthesis of PS microspheres was carried out in an emulsifier-free emulsion polymerization process, where styrene was used as the monomer after removing inhibitors, and $K_2S_2O_8$ was used as the initiator. The polymerization took place at 70°C, and the resulting PS microspheres exhibited a diameter of 660 nm with a standard deviation of 16.4 nm. Details on the synthetic conditions can be found elsewhere.[22]

The construction of PS colloidal crystals was achieved by electrophoretic deposition in a vertical arrangement. First, the PS microspheres (0.5 g) were dispersed in a solution of ethanol (100 mL) and deionized water (100 mL). A minute amount of NH_4OH was added to reach pH 10, where a stable suspension was formed. In electrophoretic depositions, the substrate was a Si wafer (4 cm^2) sputtered with 500 nm of Ti as a conductive coating. The counter electrode was a stainless steel plate (25 cm^2). The electrical field was maintained at 10 V cm^{-1}, and the deposition lasted 15 min at 26°C. Subsequently, the sample was removed and dried in air at 50°C for 10 min.

To fabricate Ni inverse opals, the PS colloidal crystals were immersed in a Ni plating solution consisting of $NiSO_4 \cdot 6H_2O$ (130 g L^{-1}), $NiCl_2 \cdot 6H_2O$ (30 g L^{-1}), and H_3BO_3 (18 g L^{-1}). The electroplating was conducted at 1 V, and its duration was adjusted between 10 and 60 min, allowing the growth of Ni structure into a desirable height. Next, the PS microspheres were carefully removed by immersing in an ethyl acetate (95 wt %) solution for 24 h at 26°C.

The electrochemical characterizations for the OER and HER were carried out in a 1 M KOH aqueous solution at 26°C using a potentiostat (Jiehan 5600). A three-electrode arrangement was adopted, where the reference and counter electrodes were Ag/AgCl and Pt (1.5 cm^2), respectively. The Ni inverse opals with a geometric area of 1 cm^2 served as the working electrode. The current–potential (*i-V*) polarizations were used at a scan rate of 5 m V s^{-1}. In addition, galvanostatic measurements were conducted at 30 mA cm^{-2} for OER and at −30 mA cm^{-2} for HER to determine the relevant lifetime and stability. Identical steps were performed on a planar Ni plate (99.5 wt %) for comparison. A scanning electron

* Electrochemical Society Active Member.
z E-mail: ppwu@mail.nctu.edu.tw

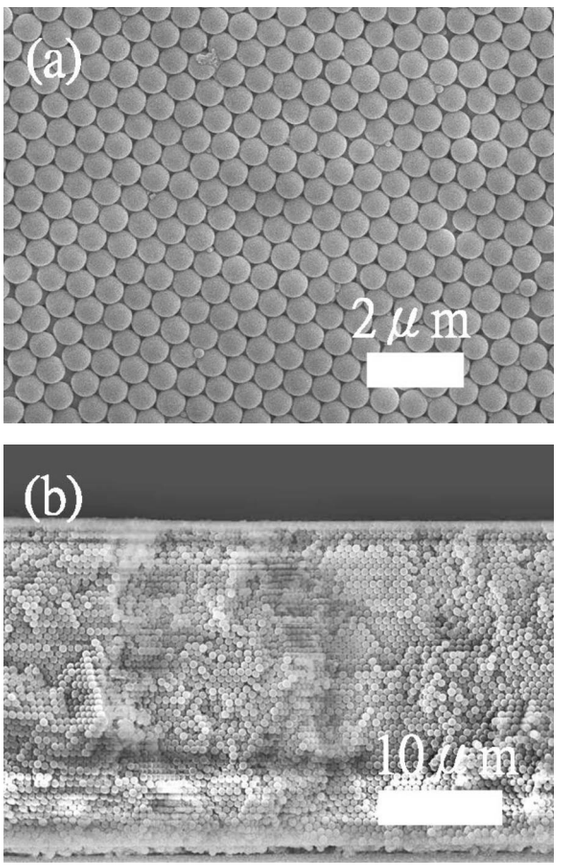

Figure 1. SEM images for PS colloidal crystals in (a) top and (b) cross-sectional views.

microscope (SEM, JEOL-JSM-6700) was employed to observe the morphologies of the colloidal crystals and Ni inverse opals. X-ray diffraction (XRD) was conducted by a Siemens D5000 with a Kα of 1.54 Å to identify the relevant Ni phase.

Results and Discussion

The SEM images in top and cross-sectional views for the PS colloidal crystals are provided in Fig. 1. As shown in Fig. 1a, the colloidal crystals revealed a close-packed face-centered cubic (fcc) (111) lattice without the appearance of vacancies, whereas the individual PS microspheres exhibited considerable size uniformities. The successful assembly of the PS microspheres was confirmed by the cross-sectional view, as shown in Fig. 1b. After 15 min of electrophoretic deposition, we were able to obtain colloidal crystals with a thickness of 26.5 μm, which corresponds to 56 layers of PS microspheres. The colloidal crystals demonstrated consistency in height without islands and valleys on the surface.

Figure 2 shows the SEM pictures for the Ni inverse opals in cross-sectional view for approximate layers of 1, 2, 3, and 7. The insets are their respective top-view images. Apparently, the Ni formed a continuous network, encompassing hexagonal arrays of pores left by PS microspheres. The size of the voids agreed with the diameter of the PS microspheres, suggesting that a swelling of the PS microspheres did not occur during the removal process. The Ni network maintained a considerable structural integrity without notable damages. Remarkably, the Ni inverse opals also displayed an impressive height consistency. This indicates that the electroplating process took place at a similar rate everywhere from the conducting layer. However, Ni overgrowths and moderate height variations were observed once the electroplating was overextended to layers

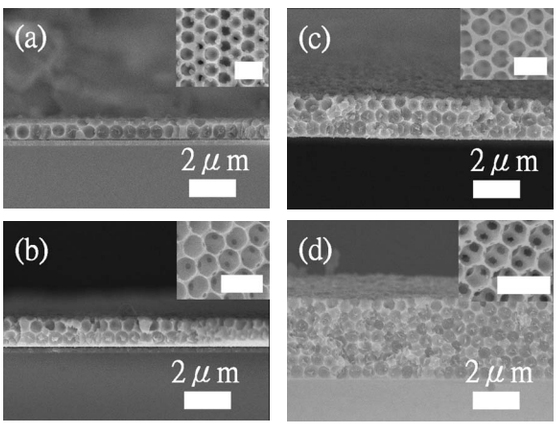

Figure 2. Cross-sectional SEM images for Ni inverse opals in (a) 1, (b) 2, (c) 3, and (d) 7 layers. The insets are their respective top views with the scale bar in 1 μm.

above 19. Hence, for electrochemical applications, the thickness for the inverse opals was limited to ~7 layers for reproducible results.

The requirement of a near-perfect arrangement for the PS microspheres is critical to our demonstration of an improved water electrolysis. It is because a randomly packed PS colloidal structure typically exhibits a significant height variation and numerous crystallographic defects. These undesirable properties would complicate the subsequent electroplating process, as both the electrolyte internal resistance loss and the Ni ion diffusion are affected by a variation in local environment. As a result, a perfect opal structure with the exact layer-by-layer control cannot be achieved. In addition, a defective arrangement of the PS microspheres leads to unnecessary thickness variation in the inverse skeleton that is likely to render structure instability from stress concentrations.[23]

Because the electrocatalytic ability is also contingent on the surface status such as crystallinity and preferred orientation, it becomes necessary to confirm the relevant phase present for the Ni inverse opals. The XRD pattern for the Ni inverse opals is displayed in Fig. 3. The diffraction peaks were identified as the (111), (200), and (220) planes. Their relative intensity was in a proper order, consistent with a polycrystalline fcc Ni (JCPDS no. 7440-02-0).

Because the OER and HER involve significant gas evolutions, adequate spaces and pathways are required to accommodate a subsequent bubble escape. In addition, electrolyte transport is another concern because its movement is likely to be interrupted by the release of bubbles. The Ni inverse opals contained interconnected pores with a diameter of 660 nm, and those pores were not linked in

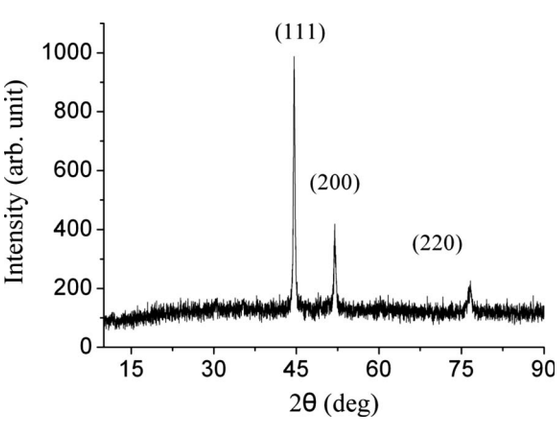

Figure 3. XRD pattern of the Ni inverse opals.

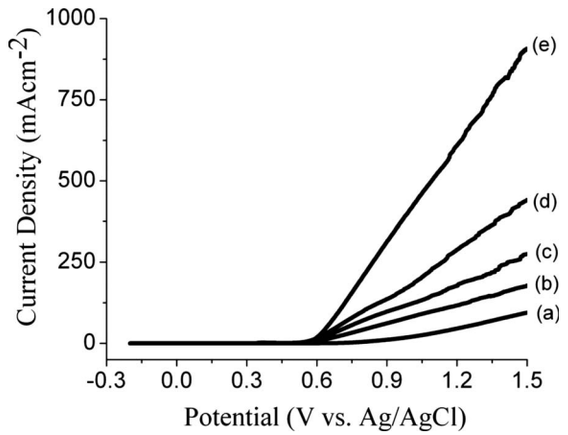

Figure 4. OER *i-V* polarization curves for (a) planar Ni plate and Ni inverse opals in (b) 1, (c) 2, (d) 3, and (e) 7 layers.

a perpendicular line. Therefore, we surmise that the catalytic abilities for the Ni inverse opals on the water electrolysis were confined to a few layers on the surface.

Figure 4 demonstrates the OER *i-V* profiles at −0.2 to 1.5 V for a planar Ni plate and Ni inverse opals in approximately 1, 2, 3, and 7 layers. The open-circuit voltage for the Ni plate and inverse opals was −0.2 V (vs Ag/AgCl). According to Medway et al., this value inferred a surface overcoat of $Ni(OH)_2$.[24] Clearly, we witnessed an obvious rise in current values when the voltage was raised above 0.6 V. Their values were proportional to the layer of Ni inverse opals. For example, at 1.5 V, the current densities from the Ni inverse opals with 1, 2, 3, and 7 layers were 178, 275, 441, and 907 mA cm^{-2}, respectively. In contrast, the Ni plate revealed a reduced current value of 94 mA cm^{-2}. Similar behaviors were observed in the HER *i-V* polarizations, as shown in Fig. 5. Notable current responses were evident at voltages negative of −1.2 V. At −1.5 V, the current densities for the Ni inverse opals with 1, 2, 3, and 7 layers were 41, 59, 95, and 206 mA cm^{-2}, respectively. As expected, the Ni plate showed a subdued current density of 21 mA cm^{-2}.

Conventional Ni-based electrodes employed for water electrolysis are sintered porous Ni and Raney Ni. Their catalytic performances are considered to be superior over those of the planar Ni plate because they exhibit a significantly larger surface area. For example, according to Hall, the sintered porous Ni electrode revealed a reduced overpotential over that of the planar one

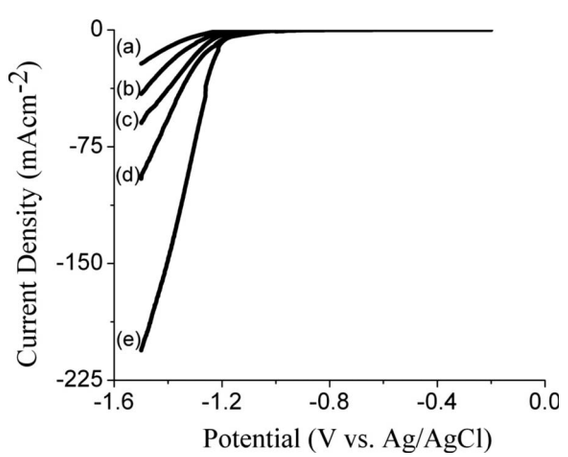

Figure 5. HER *i-V* polarization curves for (a) planar Ni plate and Ni inverse opals in (b) 1, (c) 2, (d) 3, and (e) 7 layers.

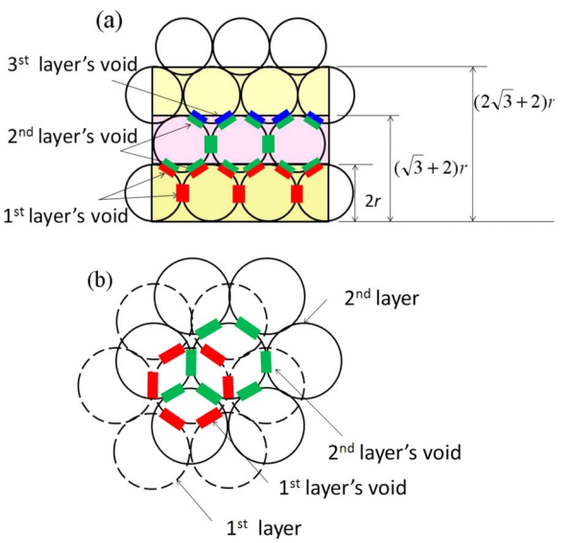

Figure 6. (Color online) Ideal colloidal crystals in (a) cross-sectional and (b) top views. The contacting areas among PS microspheres for each layer are colored for better contrast.

(∼100 mV) at 500–1500 mA cm^{-2} in a 35% KOH aqueous solution for OER.[25] The fabrication methods and their processing parameters play essential roles in determining the resulting electrode performances. In our opinion, it is simpler to select a planar Ni plate for comparison because we are primarily interested in the catalytic performances per unit geometric area (mA cm^{-2}).

Because the electrocatalytic abilities are proportional to the actual area of the electrode, further consideration in the true surface area of the Ni inverse opals is necessary to determine their effective current densities. The surface area of the inverse opals can be estimated with the following methods. The first approach was proposed by Eagleton and Searson,[26] and was later adopted by Liu et al.[27] In this method, they assumed that in an ideal inverse structure, the surface-to-volume ratio (S/V) is $\pi/2d$, where d is the diameter of the microspheres. In our case, d is 660 nm. Hence, the surface area (S) for the inverse opals can be derived by $V \times \pi/2d$. In a 1 × 1 cm footprint, the value for V can be estimated by the multiplication of the base area and the height.

In the second method, we calculate the surface area for an ideal inverse structure from the geometric consideration. A schematic diagram illustrating the cross-sectional and top views for the inverse structure is presented in Fig. 6. In a 1 × 1 cm footprint, there are 2.625×10^8 microspheres, resulting in a total surface area of 3.59 cm^2. However, the contacting areas among individual microspheres need to be subtracted because they do not contribute to the effective surface area. From the SEM images shown in the insets of Fig. 2, the contacting areas can be estimated as a disk with a radius of 150 nm. In the inverse structure of the first layer, there are nine contacting areas (six on the same plane and three above) for each PS microsphere. So the area that needs to be subtracted is $0.186 \times 9 = 1.67$ cm^2. In the second layer and above, the contacting areas for each PS microsphere became 12 (6 on the same plane, 3 above, and 3 below). Hence, the area that needs to be subtracted is $0.186 \times 12 = 2.23$ cm^2. Table I lists the values for the surface area estimated from both methods. As clearly presented, they reasonably agree with each other. To calculate the surface area for our inverse structure, we decided to adopt the method from Eagleton and Searson because their approach enables the exact determination of the surface area from direct SEM observations on the sample height.

Table II lists the estimated surface areas for our samples and the resulting effective current densities for the OER and HER from the *i-V* polarizations obtained at 1.5 and −1.5 V, respectively. For both

Table I. Comparison of the surface area for ideal Ni inverses opals in exact 1, 2, 3, and 7 layers.

Ideal inverse opals (layer)	A: $\pi/2d$[a] (cm^2)	B: Geometric consideration[b] (cm^2)	Deviation: $(B-A)/B$ (%)
1	1.57	1.92	18.2
2	2.93	3.28	10.6
3	4.29	4.64	7.5
7	9.73	10.08	3.4

[a] Method from Eagleton and Searson in Ref. 26.
[b] Method from geometric consideration, as shown in Fig. 6.

OER and HER, the effective current densities for the inverse opals were reasonably consistent with those of the planar Ni plate. At 1.5 V, the effective current densities were between 92 and 94 mA cm^{-2}. In contrast, at −1.5 V, their values were between 20 and 21 mA cm^{-2}. This large deviation in the effective current density for the OER and HER was due to their overpotential difference. In an alkaline solution, the equilibrium redox potentials for the OER and HER were 0.401 and −0.828 V, respectively. Hence, at 1.5 V, the overpotential for the OER was 1.099 V. In contrast, at −1.5 V, the overpotential for the HER was only 0.672 V. Therefore, a significant OER current was observed over that of HER. In addition, during the OER, Ni was prone to inherent oxidation, and that might also contribute some residue currents.

From both the OER and HER *i-V* polarization curves, we realized that the Ni inverse opals of three layers exhibited a better compromise between the increase in the surface area and the difficulty of bubble (H_2/O_2) escape. Hence, the lifetime evaluation was carried out on the Ni inverse opals of three layers, and the results are displayed in Fig. 7. For the OER, both the Ni plate and the inverse opals demonstrated stable curves starting at voltages of 0.706 and 0.6 V, respectively. These values reasonably agreed with earlier *i-V* polarization curves shown in Fig. 4. However, for the HER, the voltages started at −1.48 and −1.2 V. The observed voltage fluctuations were due to the interference from gas release, as the attachment of bubbles not only increased the ohmic resistance in the electrolyte but also decreased the catalytic surface areas.[28,29] The planar Ni plate revealed a larger voltage fluctuation than the inverse opals for both the OER and HER. Unfortunately, the exact nature for this behavior is still unknown. On average, water electrolysis using the Ni plate and inverse opals at 30 mA cm^{-2} demonstrated overpotentials of 1.049 and 0.94 V, respectively.

The SEM images after galvanostatic measurements on the Ni inverse opals confirmed structural stabilities without notable damages. This unique mechanical strength might come from the fcc close-packed arrangements. Our results indicated that an increase in the electrochemical surface area in a limited footprint can be realized by the fabrication of inverse opals. With suitable macropores, the inverse opals allow facile mass transports in the entire physical area that not only renders a reduced overpotential but also leads to catalytic stability. This is in sharp contrast to the conventional designs of nanostructured electrodes, where substantial amounts of area were determined inaccessible due to mass transport limitation.[30,31] For example, a recent work by Kim et al. on the RuO_2 nanorod array indicated that only the cap portions were useful for water electrolysis.[31] We realized that, in the long run, the Ni inverse opals would not be suitable for the OER because of the instability in an alkaline electrolyte. However, the Ni structure is certainly applicable for the HER. In addition, further performance enhancement is likely once known catalytic nanoparticles are impregnated onto the Ni inverse platform. Lastly, we emphasize that a direct cost comparison with that of a sintered porous Ni electrode would not be favorable for the Ni inverse structure because the fabrication steps involved in the inverse structure are more complicated and time-consuming. Nevertheless, the Ni inverse structure might be useful for the miniaturized water electrolysis cell because the Si substrate is more compatible with existing microelectromechanical system manufacturing protocols, and electrophoresis and electroplating can be properly scaled down.

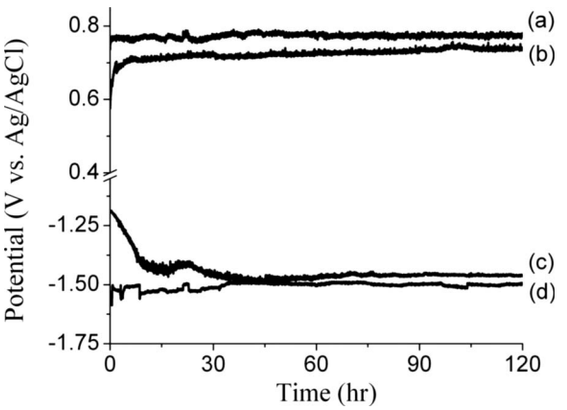

Figure 7. Galvanostatic profiles for OER in (a) planar Ni plate and (b) Ni inverse opals of three layers, as well as HER in (c) Ni inverse opals of three layers and (d) planar Ni plate.

Conclusion

The fabrication of Ni inverse opals was successfully achieved by the construction of PS colloidal crystals via a vertical electro-

Table II. The actual surface area for the Ni inverse opals and corresponding effective current densities for the OER and HER.

			OER		HER	
Sample	Height (μm)	Surface area[a] (cm^2)	Measured current[b] (mA cm^{-2})	True current[c] (mA cm^{-2})	Measured current[d] (mA cm^{-2})	True current[e] (mA cm^{-2})
Ni plate	N/A	1	94.7	94.7	21.7	21.7
1 layer	0.82	1.954	178.6	91.4	41.1	21.0
2 layers	1.25	2.979	275.3	92.4	59.6	20.0
3 layers	2.0	4.766	441.6	92.7	95.5	20.0
7 layers	3.8	9.955	907.2	91.1	206	20.7

[a] Surface area estimated from the method provided in Ref. 26 with SEM determined height.
[b] Current densities determined at 1.50 V (vs Ag/AgCl).
[c] Values obtained from dividing the measured current densities by estimated surface area.
[d] Current densities determined at −1.50 V (vs Ag/AgCl).
[e] Values obtained from dividing the measured current densities by estimated surface area.

phoretic deposition, followed by potentiostatic electroplating and chemical removal of PS microspheres. By adjusting the processing parameters, we obtained inverse opals in multiple layers with considerable surface uniformities. Responses from the *i-V* polarizations indicated that the catalytic abilities for the OER and HER increased with the layers of inverse opals. The calculations of the effective current densities determined that the entire area of the inverse opals was accessible for electrochemical reactions. In lifetime performance, the inverse opals demonstrated reasonably stable voltage profiles for 120 h with a negligible degradation for both OER and HER.

Acknowledgments

The authors are grateful to Professor Pang Lin and Professor George Tu for their kind assistance with the laboratory equipment. The financial support from the National Science Council of Taiwan (98-2221-E-009-040-MY2) is acknowledged.

National Chiao Tung University assisted in meeting the publication costs of this article.

References

1. Y. Cai, A. B. Anderson, J. C. Angus, and L. N. Kostadinov, *Electrochem. Solid-State Lett.*, **8**, E62 (2005).
2. M. J. Cuetos, X. Gómez, A. Escapa, and A. Morán, *J. Power Sources*, **169**, 131 (2007).
3. R. K. Shervedani and A. Lasia, *J. Electrochem. Soc.*, **144**, 511 (1997).
4. W. Hu, *Int. J. Hydrogen Energy*, **25**, 111 (2000).
5. Y. L. Lo and B. J. Hwang, *J. Electrochem. Soc.*, **143**, 2158 (1996).
6. B. Chi, H. Lin, and J. Li, *Int. J. Hydrogen Energy*, **33**, 4763 (2008).
7. M. S. El-Deab, M. I. Awad, A. M. Mohammad, and T. Ohsaka, *Electrochem. Commun.*, **9**, 2082 (2007).
8. J. Y. Huot, M. L. Trudeau, and R. Schulz, *J. Electrochem. Soc.*, **138**, 1316 (1991).
9. S. A. Grigoriev, P. Millet, and V. N. Fateev, *J. Power Sources*, **177**, 281 (2008).
10. R. K. Shervedani and A. Lasia, *J. Electrochem. Soc.*, **144**, 2652 (1997).
11. R. N. Singh, D. Mishra, Anindita, A. S. K. Sinha, and A. Singh, *Electrochem. Commun.*, **9**, 1369 (2007).
12. J. E. G. J. Wijnhoven, S. J. M. Zevenhuizen, M. A. Hendriks, D. Vanmaekelbergh, J. J. Kelly, and W. L. Vos, *Adv. Mater.*, **12**, 888 (2000).
13. H. Yan, C. F. Blanford, B. T. Holland, M. Parent, W. H. Smyrl, and A. Stein, *Adv. Mater.*, **11**, 1003 (1999).
14. X. Yu, Y. J. Lee, R. Furstenberg, J. O. White, and P. V. Braun, *Adv. Mater.*, **19**, 1689 (2007).
15. Y. Y. Song, D. Zhang, W. Gao, and X. H. Xia, *Chem.-Eur. J.*, **11**, 2177 (2005).
16. Y. Liu, J. Chen, V. Misoska, G. S. Swiegers, and G. G. Wallace, *Mater. Lett.*, **61**, 2887 (2007).
17. T. Teranishi, M. Hosoe, T. Tanaka, and M. Miyake, *J. Phys. Chem. B*, **103**, 3818 (1999).
18. N. Chandrasekharan and P. V. Kamat, *Nano Lett.*, **1**, 67 (2001).
19. K. Luo, N. Shi, H. Cong, and C. Sun, *J. Solid State Electrochem.*, **10**, 1003 (2006).
20. Y. J. Huang, C. H. Lai, and P. W. Wu, *Electrochem. Solid-State Lett.*, **11**, P20 (2008).
21. Y. J. Huang, C. H. Lai, P. W. Wu, and L. Y. Chen, *Mater. Lett.*, **63**, 2393 (2009).
22. C. E. Reese and S. A. Asher, *J. Colloid Interface Sci.*, **248**, 41 (2002).
23. A. Y. Zaitsev, D. S. Wilkinson, G. C. Weatherly, and T. F. Stephenson, *J. Power Sources*, **123**, 253 (2003).
24. S. L. Medway, C. A. Lucas, A. Kowal, R. J. Nichols, and D. Johnson, *J. Electroanal. Chem.*, **587**, 172 (2006).
25. D. E. Hall, *J. Electrochem. Soc.*, **132**, 41C (1985).
26. T. S. Eagleton and P. C. Searson, *Chem. Mater.*, **16**, 5027 (2004).
27. Z. Liu, Z. Jin, J. Qiu, X. Liu, W. Wu, and W. Li, *Semicond. Sci. Technol.*, **21**, 60 (2006).
28. D. Kiuchi, H. Matsushima, Y. Fukunaka, and K. Kuribayashi, *J. Electrochem. Soc.*, **153**, E138 (2006).
29. T. Iida, H. Matsushima, and Y. Fukunaka, *J. Electrochem. Soc.*, **154**, E112 (2007).
30. P. C. Chen, Y. M. Chang, P. W. Wu, and Y. F. Chiu, *Int. J. Hydrogen Energy*, **34**, 6596 (2009).
31. S. Kim, N. Koratkar, T. Karabacak, and T. M. Lu, *Appl. Phys. Lett.*, **88**, 263106 (2006).